Inkless Multimaterial Printing Flexible Electronics by Directed Laser Deposition at Nano and Microscale

*Zabihollah Ahmadi,[1] Aarsh Patel,[1] Adib Taba, [1] Suman Jaiswal, [1] Seungjong Lee,[2,3] Nima Shamsaei,[2,3] Masoud Mahjouri-Samani[1,3]**

[1]Electrical and Computer Engineering Department, Auburn University, Auburn, AL 36849, USA.
[2]Department of Mechanical Engineering, Auburn University, Auburn, AL 36849, USA.
[3]National Center for Additive Manufacturing Excellence (NCAME), Auburn University, Auburn, AL 36849, USA.
*Corresponding author: Mahjouri@auburn.edu

Abstract

Additively manufactured electronics (AMEs), also known as printed electronics, are becoming increasingly important for the anticipated Internet of Things (IoT). This requires manufacturing technologies that allow the integration of various pure functional materials and devices onto different flexible and rigid surfaces. However, the current ink-based technologies suffer from complex and expensive ink formulation, ink-associated contaminations (additives/solvents), and limited sources of printing materials. Thus, printing contamination-free and multimaterial structures and devices is challenging. Here, a multimaterial additive nanomanufacturing (M-ANM) technique utilizing directed laser deposition at the nano and microscale is demonstrated, allowing the printing of lateral and vertical hybrid structures and devices. This M-ANM technique involves pulsed laser ablation of solid targets placed on a target carousel inside the printer head for in-situ generation of contamination-free nanoparticles, which are then guided via a carrier gas toward the nozzle and onto the surface of the substrate, where they are sintered and printed in real-time by a second laser. The target carousel brings a particular target in engagement with the ablation laser beam in predetermined sequences to print multiple materials, including metals, semiconductors, and insulators, in a single process. Using this M-ANM technique, various multimaterial devices such as silver/zinc oxide (Ag/ZnO) photodetector and hybrid silver/aluminum oxide (Ag/Al_2O_3) circuits are printed and characterized. The quality and versatility of our M-ANM technique offer a potential manufacturing option for emerging IoT.

Keywords: printed electronics, multimaterial printing, additive nanomanufacturing, dry printing, flexible hybrid electronics.

Introduction

With the emergence of the Internet of Things (IoT), where most objects and systems are anticipated to be made smart, there is great interest in developing new materials and advanced manufacturing techniques in order to integrate various functionalities, including sensors, batteries, displays, and electronics directly onto different surfaces [1-6]. Conventional electronics manufacturing approaches such as photolithography, focus ion beam (FIB), and electron beam lithography (EBL) require sophisticated and expensive cleanroom facilities or high vacuum equipment and further involve multiple subtractive steps. Thus, there is a wide interest in cost-effective additive manufacturing/printing technologies that can work in atmospheric conditions and print on various surfaces.

Printed flexible electronic devices are often lightweight, bendable, stretchable, and wearable, with potential applications in healthcare, energy, aerospace, and defense industries [7-9]. Currently, flexible electronics are mostly fabricated with a single material in a single layer [10-15]. Most devices and structures with sophisticated functionalities, such as electronics, optoelectronics, and sensors, typically require multimaterial deposition. Thus, there are emerging needs for printing methods that allow multimaterial printing in multilateral configurations.[16]

The current state-of-the-art printed electronics mostly revolve around ink-based manufacturing techniques such as inkjet and aerosol jet printing (IJP and AJP) [17-20]. These direct printing methods overcome the challenges of conventional lithography-based processes, which require expensive manufacturing facilities with complex and wasteful processes [6, 21-32]. IJP and AJP techniques have been successful in printing a limited single material in a single process step. A few printing methods have also been reported that are capable of printing multimaterials [33-39]. For example, Skylar-Scott et al.[40] reported a micrometer-scale printing strategy by fast switching between viscous materials which are extruded through a single nozzle. Wanjun Liu et al.[41] developed an extrusion-based multimaterial bioprinting platform capable of depositing multiple coded bio-inks in a continuous manner by switching between different reservoirs. Ke Sun et al.[42] showed 3D interdigitated microbattery architectures by printing concentrated lithium oxide-based inks. Although these extrusion-based printing methods have been used to fabricate functional devices [42-48], the construction of multimaterial architectures often involves sequentially printing individual materials using multiple nozzles. Besides the limited availability of the source materials for printing, the drawbacks of printing one material at a time include the need for careful alignment of each nozzle as well as start-and-stop ink flow on demand without introducing defects [49, 50].

Ink-based printing techniques have several other disadvantages as well. The ink formulation is complex, and developing individual functional ink requires extensive effort, time, and cost. For example, preparing a functional ink requires multiple steps, including nanoparticle preparation, nanoparticle suspension in a solution, particle dispersion, centrifugation, homogenization, and controlling the adhesion and viscosity of inks [49]. Thus, multimaterial printing is mainly limited to non-functional materials due to the trade-off between ease of processing and functionality [51]. Also, using solvents and additives for tuning the concentration of the inks requires additional surfactant removal and thermal annealing steps, which complicates the device manufacturing process [52, 53]. Moreover, in solvent-based printing methods, only materials that are soluble in the printing solvent can be used. However, many functional materials do not dissolve in common solvents, significantly limiting material selection. The solvent, additives, and polymers commonly used in the inks formulation make achieving high conductivity in ink-based printed materials challenging. The presence of impurities from the ink introduces variability in the printing conductivity, making these techniques less repeatable.

New technology is therefore needed to print fully functional, pure multimaterial structures and devices using a single printer and in a single process step. Thus, there has been an extensive effort to find alternative printing methods, such as laser-induced forward transfer (LIFT)[54], for printing multimaterials. However, this technique requires rigorous source sample preparation, which is usually a liquid-based coating process. It also needs delicate instrumentation for the transfer process resulting in splash/cracking issues as well as scaling-up and yield challenges.

Here we introduce multimaterial additive nanomanufacturing (M-ANM) and dry printing technology for printing various pure materials and hybrid structures in a single print. This method can eliminate the need for assembly, reduce the need for post-processing, and promote the efficient design of multifunctional devices. This particle-by-particle and layer-by-layer printing approach is capable of printing various materials by switching between the target materials in a single run during the print process. The M-ANM is a laser-based technique that generates nanoparticles on-demand and in situ by pulsed laser ablation of solid targets. The generated nanoparticles inside the printer head are then guided toward the nozzle and onto the surface of the substrate by a gas flow, where they are sintered and printed in real-time by a second laser. A target carousel holding multiple targets is rotated to bring a particular target into engagement with the ablation laser beam when needed. The rotation of the targets in predetermined sequences allows the printing multiple materials onto the substrate in a single process step. For instance, here, we show the printing of hybrid multimaterial structures using various materials such as barium titanate (BTO), titanium dioxide (TiO_2), tin oxide (SnO), zinc oxide (ZnO), aluminum oxide (Al_2O_3), and silver (Ag). In addition, to demonstrate the capability of the M-ANM system, fully printed multimaterial devices such as Ag/ZnO photodetectors and Ag/Al_2O_3 electronic circuits are prepared and tested.

This M-ANM technique is thus highly efficient as it does not use ink, does not need post-processing, and does not have ink-associated contaminations. Also, it is more cost-effective, and the target shelf-life is much longer than ink. Also, in contrast to regular cleaning of the ink-based printers after each use, the M-ANM technique rarely requires cleaning, and the printing speed is also comparable with inkjet and aerosol jet methods.

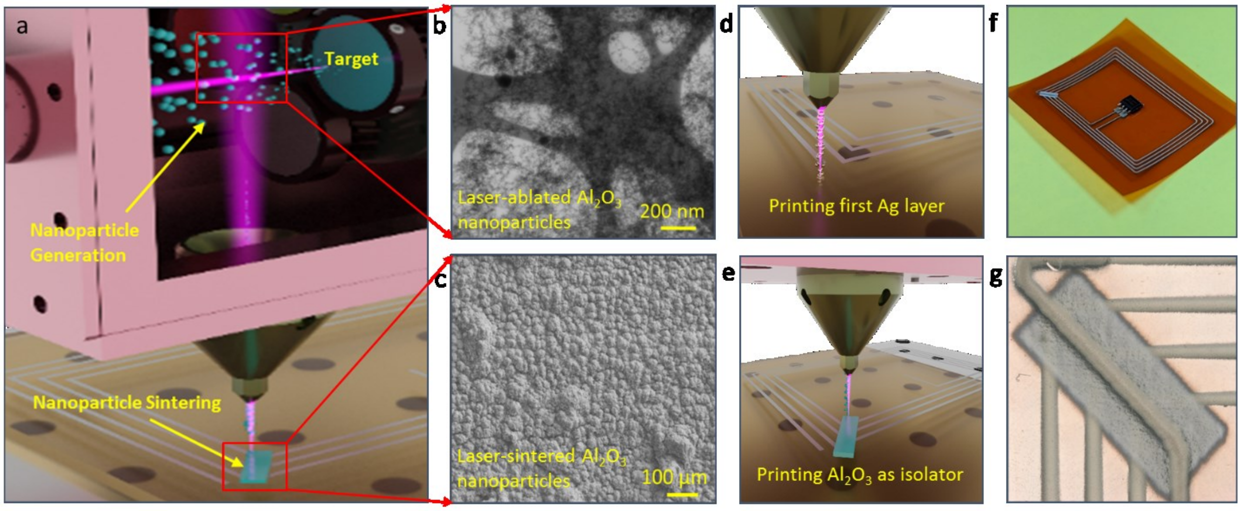

Figure 1. Schematic illustration of the multimaterial additive nanomanufacturing (M-ANM) and dry printing method (**a**). TEM image showing an example of laser-generated nanoparticles inside the printer head (b). SEM image showing an example of laser-sintered nanoparticles as they land on the substrate during the print process (c). An example of the process flow for printing a multimaterial conductor/insulator (Ag/Al_2O_3) hybrid structure (**d, e**). First, Ag antenna pattern is printed on the polyimide substrate (**d**). The Al_2O_3 layer is printed on a section of the Ag lines as an isolating bridge layer (**e**) followed by printing Ag crossing over the top of the Al_2O_3 layer to complete the NFC antenna device. Photograph of a completed circuit with a M24LR04E IC chip mounted on the printed antenna (**f**). Close-up optical image of the printed insulating Al_2O_3 bridge with the crossed Ag lines (**g**).

Experimental Section

A schematic representation of the dry printing M-ANM method is shown in **Figure 1a**. This dry multimaterial printer consists of a nanoparticle generation chamber, a nozzle, a target carousel holding multiple targets inside the chamber, a pulsed laser for target ablation and nanoparticle generation, a gas flow system, and a second laser for sintering the nanoparticles as they land on the substrates placed on an XY stage under the nozzle.

To demonstrate multimaterial printing, we first printed a silver-based NFC tag antenna with Al_2O_3 as the isolating layer. Most electronic circuits require cross-over conductive lines to complete a circuit. For this purpose, insulators have to be printed between the cross-over conductive lines to avoid electrical shorting. In this example, we used silver as the conductive material and Al_2O_3 as the insulating material. First, the target carousel was adjusted to position the Ag target for laser ablation and nanoparticle generation process. The nanoparticle generation involved pulsed laser ablation and the formation of a laser plasma followed by the plume condensation in high argon background gas. When a pulsed laser beam with a high peak power interacted with the surface of the materials, it led to rapid heating and vaporization and the formation of a plasma plume. The interaction of the plume with the background gas resulted in the condensation of the plume and the formation of nanoparticles, as shown in **Figure 1b**.

The nanoparticles were guided toward the substrate through the nozzle using an argon gas flow. These nanoparticles were then laser sintered on the flexible polyimide substrate in real-time, as shown in **Figure 1c**. While most nanoparticles transferred through the nozzle and subsequently deposited and sintered on the substrate, a portion of the nanoparticles was adhered to the chamber walls over time, which could be readily cleaned and wiped away. After printing the first predesigned Ag layer (**Figure 1d**), the nanoparticle generation stopped, and the printer head was quickly pumped to remove the residual silver nanoparticles. Then target carousel was rotated to bring the Al_2O_3 target in position for nanoparticle generation and subsequent printing processes (**Figure 1e**). Finally, for printing the third layer Ag line crossing the insulator bridge, the printer head was quickly pumped, and the target carousel rotated back to position the Ag target for nanoparticle generation and printing processes. The NFC tags are magnetically coupled by inductive loop antennas. A battery is not required to access the tag, whether in write or read mode, since the tag harvests the energy needed to operate from the electromagnetic field generated by the reader. **Figure f** shows the completed circuit where the M24LR04E IC is mounted on the printed circuit. **Figure S1a-c** shows the optical images of the printed antenna at different printing stages. The mounted M24LR04E IC was programmed to launch the group's website when brought to the proximity of a cellphone with NFC system (**Video S1**). **Figure 1g** show the close-up optical images of the isolating Al_2O_3 layer between crossed Ag lines and the flexibility of NFC antenna, respectively.

The commercially available nozzles used in our system had a diameter ranging from 100 µm up to a few millimeters. The line-width resolution in these experiments was limited to the commercially available nozzles used in this work. In should be noted that the resolution could be further enhanced by using smaller diameter or aerodynamic focusing nozzles, enabling sub-10 µm resolutions. All the samples were printed at room temperature and atmospheric pressure onto ~127 µm thick polyimide substrates. The substrates were located ~1 mm below the nozzle tip, and the gas flow rate was kept at ~1000 sccm constant during all experiments. The laser source for ablation was a 60 W pulsed fiber laser (1064 nm) with ~1 mJ energy per pulse. The ablation laser beam was focused on the surface of the targets through a laser galvo scanner having a laser spot of ~50 microns. For laser ablation of the Ag and Al_2O_3 targets, 24 and 21W laser powers were used, respectively. The pulse repetition rate and scan speed were set to 30 KHz rate and 1000 mm/s. The ablation laser power for laser ablation of the ZnO and SnO was set to 9W, and for TiO_2 and BTO targets was set to 15 W. These values were chosen by experimental observation to ensure ablation takes place and particle generation is sufficient for the printing process while avoiding excessive particle generation and clogging the nozzle.

The sintering process was performed using a 20W 1064nm pulsed nanosecond fiber laser. For the sintering and printing of Ag nanoparticles, 10 mm/s printing speed and ~0.9 W laser power were used. The al_2O_3 layer was printed using 20 mm/s printing speed and ~1.13 W laser power. ZnO was printed using 10mm/s, ~0.6 W. For the BTO, SnO, and TiO_2, the laser power was ~0.11, ~0.4, and ~0.12 W, respectively, with a 10 mm/s printing speed for all.

Finding the optimal laser power for a given printing speed was a critical step that required careful experimentation. In addition, the laser power and printing speed had to be balanced. This is because increasing the printing speed reduced the amount of time available for the generated nanoparticles to deposit on the substrate. Also, as the laser moved more quickly across the substrate, there was less time for the laser energy to heat and sinter the nanoparticles deposited on the substrates. Thus, the laser power needed to be increased to achieve the same printing quality at lower speeds and sintering laser powers. As shown in our previous studies [22, 23], the thickness of deposited materials was also proportional to the gas flow rate and the number of printing layers. Higher gas flow rate transfers more ablated particles per second onto the substrates, resulting in a thicker deposition for the same process parameters.

It should be mentioned that the size of laser-ablated nanoparticles may be tuned using various process parameters. The laser fluence, wavelength, pulse width, material properties, and background pressure can all affect the size of the ablated nanoparticles. For instance, generating more ablated flux (e.g., with higher laser fluence) and higher background pressure leads to more condensation hence larger particle formation and vice versa.

Results and Discussions

The laser-generated nanoparticles were studied by scanning transmission electron microscopy (STEM) to confirm the nanoparticles' formation and get a better insight into the size and shape of the generated nanoparticles, such as BTO, TiO_2, SnO, and ZnO, as shown in **Figure 2a-d**, respectively. In general, the nanoparticles were in the order of ~3 to 10 nm in diameter. The scanning electron microscopy (SEM) images in **Figure 2e-h** show the deposited and laser-sintered BTO, TiO_2, SnO, and ZnO nanoparticles, respectively.

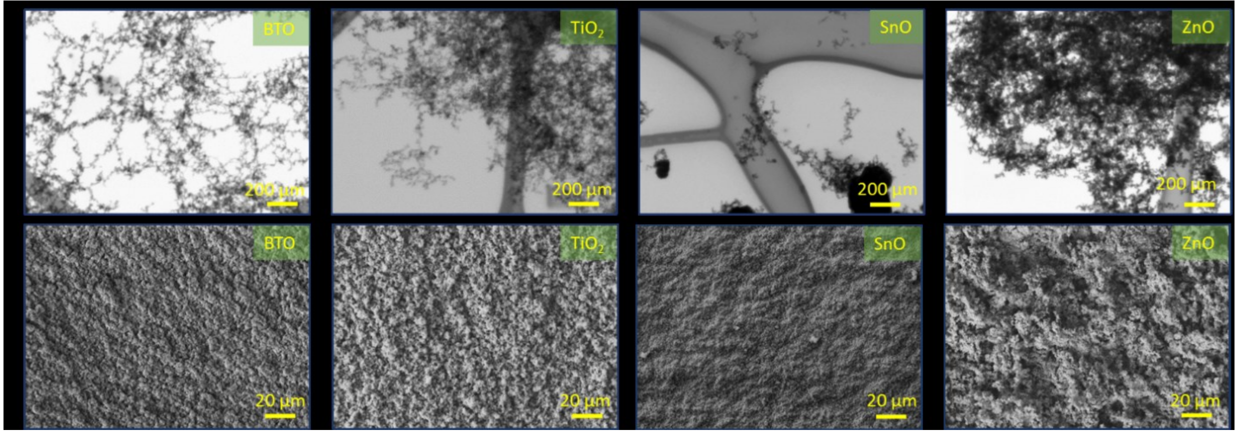

Figure 2. STEM images of BTO (**a**), TiO_2 (**b**), SnO (**c**), and ZnO (**d**) nanoparticles generated by M-ANM printer. SEM images of BTO (**e**), TiO_2 (f), SnO (**g**), and ZnO (**h**) sintered by ANM printer.

The effect of laser sintering on the crystallization and sintering of BTO, TiO_2, SnO, and ZnO nanoparticles was further studied by Raman and X-ray spectroscopy methods, as shown in **Figure 3**. After the sintering process, the Raman spectra clearly showed the characteristics vibrational modes of the samples. For instance, the Raman modes of the sintered BTO samples were observed at 260 cm^{-1}, 302 $cm^{-1,}$ and 717 cm^{-1}, representing the crystalline characteristics of the samples (**Figure 3a**). Similarly, the Raman active modes of TiO_2 crystals, including 137 cm^{-1}, 386 $cm^{-1,}$ and 625 cm^{-1} (**Figure 3b**) were observed, indicating the anatase phase of the crystallized TiO_2 samples. The Raman spectrum of SnO showed the A_{1g} phonon mode at ~204 cm^{-1} (**Figure 3c**), and ZnO showed the representative Raman modes at 435 cm^{-1} and 574 cm^{-1} (**Figure 3d**). **Figure 3e-h** demonstrates the X-ray spectra of sintered BTO, TiO_2, SnO, and ZnO, respectively, reconfirming the crystallinity of the sintered nanoparticles.

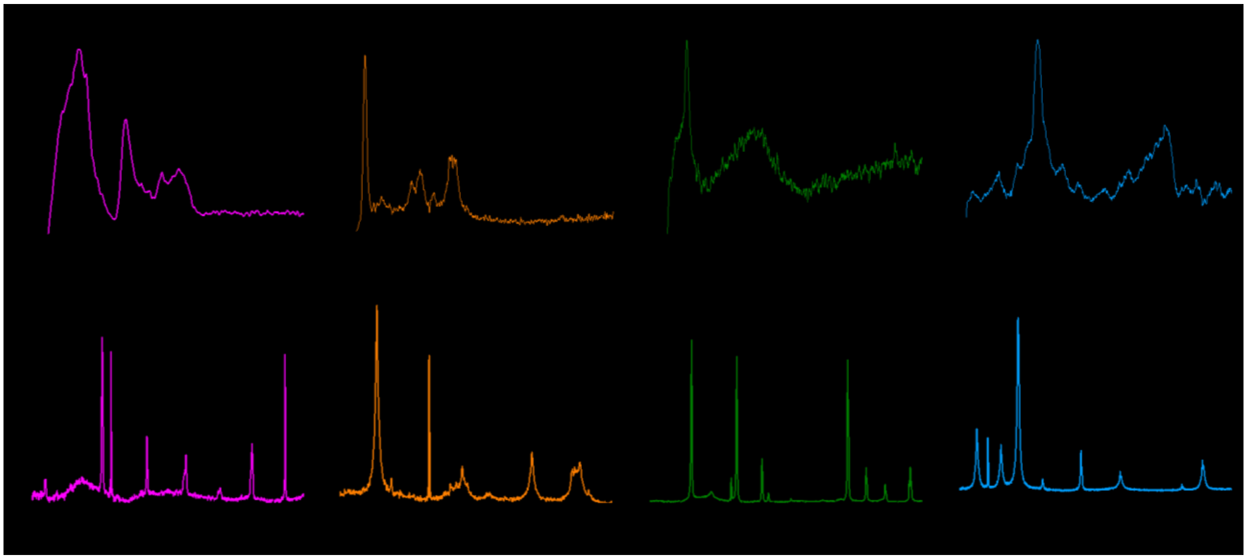

Figure 3. Raman spectra of sintered BTO (**a**), sintered TiO_2 (**b**), sintered SnO (**c**), and sintered ZnO (**d**). XRD plots of sintered BTO (**e**), sintered TiO_2 (**f**), sintered SnO (**g**), and sintered ZnO (**h**).

The versatility of the M-ANM technique enabled us to directly print multiple materials onto the desired location, either side-by-side or in a layer-by-layer configuration. As an example, the Ag-SnO-ZnO heterojunctions were printed side-by-side, as shown in **Figure 4a**. The close-up views of the junctions are shown in **Figure 4b-d**. Also, as shown in **Figure 4e and f**, BTO/ZnO/TiO_2, and BTO/ZnO/SnO patterns were printed on polyamide substrates by rotating the target carousel to bring a particular target into position for nanoparticle generation and sintering processes. The measured thickness of printed ZnO, Ag, BTO, SnO and TiO_2 are ~ 1.3 µm, 1.5 µm, 10 µm, 4.3 µm and 45 µm, respectively. The SEM cross-section of the TiO_2-Ag multilayer produced by the M-ANM technique is presented in **Figure 4g**. Energy dispersive spectroscopy (EDS) element maps shown in **Figure 4h-j** indicate the capability of heterostructures formation made of multiple materials with clear boundaries.

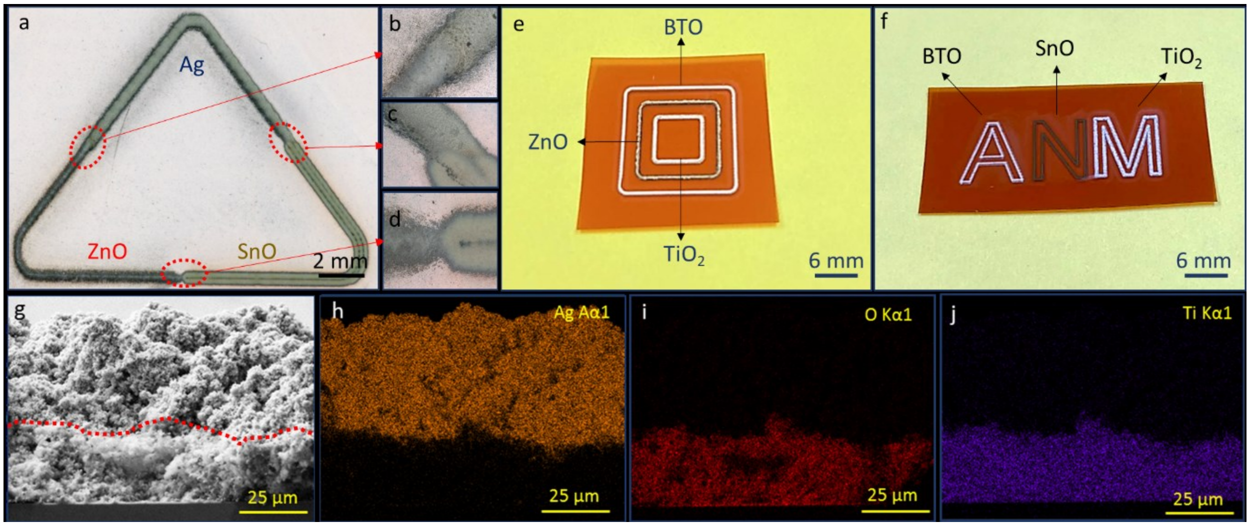

Figure 4. Optical image of side-by-side M-ANM printed Ag-SnO-ZnO lines (**a**). Optical images of Ag-ZnO (**b**), ZnO-SnO (**c**) and Ag-SnO (**d**) junction. (**e, f**) Optical images of BTO, ZnO, and TiO_2 printed on polyamide in a single run. Cross-section of printed Ag on top of TiO_2 (**g**). EDS elemental maps of printed TiO_2/Ag hybrid structure layer-by-layer (**h-j**).

To understand the correlation between the number of printed layers and the thickness of the printed lines, their height profiles were measured and analyzed using a KEYENCE optical microscope. The thickness of printed materials could be increased by adding more printing layers, as this led to the higher deposition of material layer-by-layer. Conversely, reducing the number of printing layers resulted in thinner printed lines. Additionally, higher printing speeds resulted in less material deposition, while lower printing speeds generally led to higher material deposition.

As shown in **Figure 5a**, by increasing the number of printed passes, the thickness of the printed lines could simply be adjusted. For instance, increasing the number of printed passes from 10 to 100 layers resulted in thicknesses ranging from ~1 to 16 microns. **Figure 5b** represents the resistance of the printed Ag lines as a function of printed pass numbers. The lines resistance decreased by increasing the number of printed passes and hence increasing the thickness of the printed lines. Based on the results from **Figure 5a, b,** we achieved resistivity as low as $\sim 1\times10^{-7}$ Ω m at a thickness of ~1 µm.

Repeated cycling/bending can cause strain on the printed materials and can change the microstructure and thus affecting the resistance of printed materials. In addition to that, cracks can be initiated in the printed materials under different strains, which can also contribute to changes in resistance. Therefore, it is critical to consider the potential effects of repeated cycling/bending on printed materials for different applications. Here, the mechanical stability, structural durability, and electrical properties of the printed lines were characterized by performing bending and cycling tests (**Figure 5c-e**). The cycling test on a series of 10 mm printed Ag lines on $12\times4\times0.127$ mm^3 polyimide substrates was performed using a custom-made bending system (**Figure 5f**). The initial and final resistance of printed lines at different strains (0.32 to 0.53%) and cycling numbers (10^4, 10^5, and 10^6) were measured and plotted, as shown in **Figure 5c-e**. The results show slight changes in the resistance of printed Ag at different strains and cycles, which confirms well-sintered Ag nanoparticles together and good adhesion of the printed materials to the substrate.

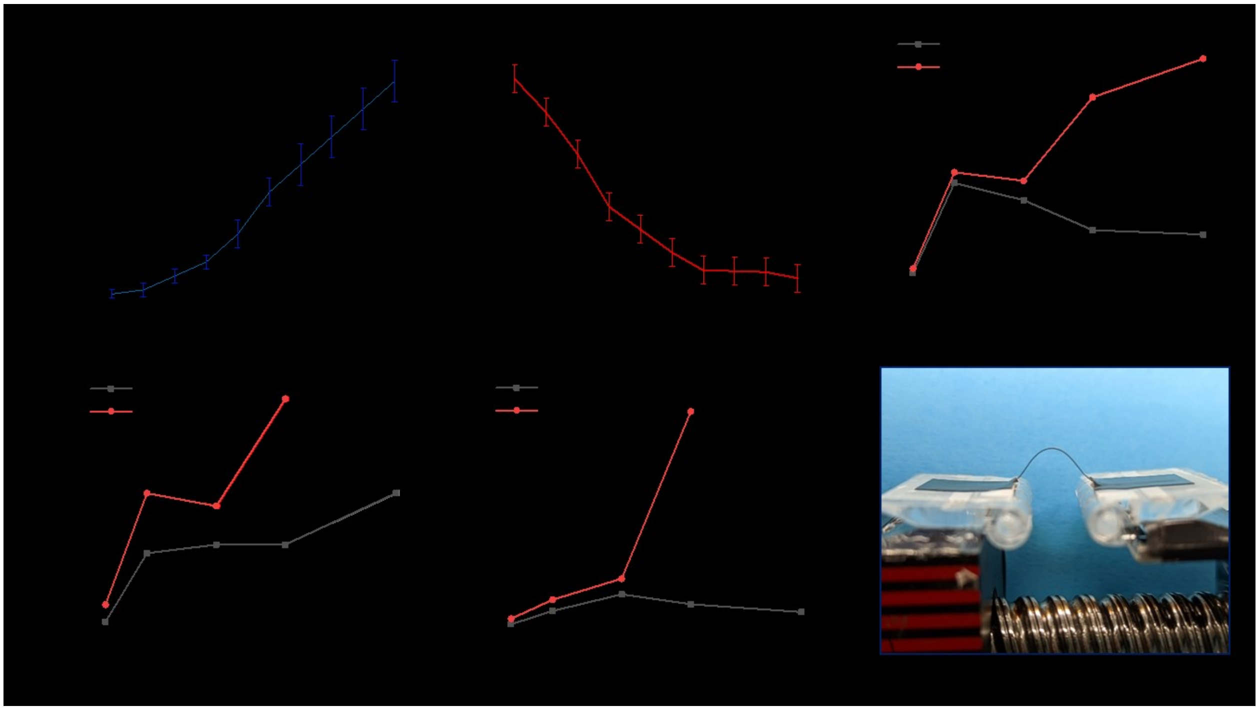

Figure 5. Thickness (**a**) and resistance (**b**), plots as a function of the number of printed layers ranging from 10 to 100 passes. Initial and final resistances of the printed Ag-lines under various strains and cycles, including 10^4 (**c**), 10^5 (**d**), and 10^6 (**e**) cycles. Digital photo of custom-made bending and cycling machine (**f**).

To demonstrate the multimaterial printing capability of the approach, various devices were designed, printed, and tested. For instance, since photodetectors are an important class of optoelectronic devices and sensors that translate optical information into an electrical readout [55], we printed an array of Ag-ZnO photodetectors printed on flexible polyimide substrate, as shown in **Figure 6a-c** with 2D and 3D optical images. First, Ag electrodes were printed, followed by switching the target and printing ZnO. The electrical and optoelectronic performances of the fabricated photodetectors were measured by a semiconductor characterization system (Keithley 2400) under controlled UV LED (0.6 W@405 nm) illumination. All measurements were performed at atmospheric pressure and at room temperature. The UV LED was turned on and off at 0.5 Hz frequency. As shown in **Figure 6d, e**, the photocurrent spontaneously increased upon UV irradiation under different voltage biases (1-5V) and different illumination power densities (0.15 to 0.55W/cm^2). The device exhibited good flexibility and stability even after bending under different strains (**Figure 6f, g**). The UV intensity dependence in **Figure 6h** shows linearity over the power density from 0.15 to 0.55 W/cm^2, and the sensitivity is measured as 0.6 µA per 0.1 W/cm^2.

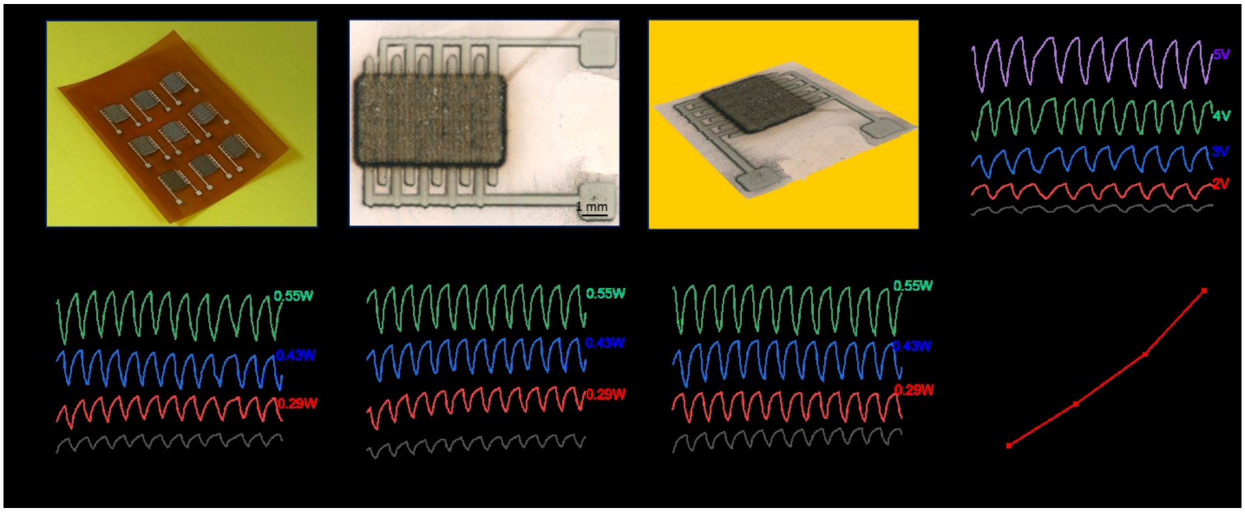

Figure 6. Digital photo of flexible Ag-ZnO photodetector arrays (**a**). 2D (**b**) and 3D (**c**) optical images of printed ZnO-based photodetector. Photoresponses of the sensor under various biased voltages (**d**) and light intensities (**e**). Photoresponses of the ZnO photodetector under various illumination intensities under different strains (**f**, **g**). Peak current of photodetector as a function of power density(**h**).

Another significant challenge in printed electronics is to create line cross-overs without shorting the circuit [56]. This requires a multimaterial printing capability for printing an insulating layer between the conducting lines. **Figure 7a** shows an example of a printed multimaterial flexible electronic circuit on polyimide using Ag lines as a conductive layer and an Al_2O_3 layer as a dielectric isolator. To print this device, we designed and printed the first Ag layers (Supporting Information **Figure S2a**). The Ag lines exhibited a resistivity of ~$1.2\times10^{-7}\Omega$ m. By rotating the target from Ag to Al_2O_3, the Al_2O_3 dielectric layer was printed on the pre-defined locations to electrically isolate the crossed Ag lines (Supporting Information **Figure S2b**). Finally, the Ag lines were printed on the desired location and crossed over the insulating layers to complete the circuit (Supplementary **Figure S2c**). The 3D view image and height profile in **Figure 7b, c** shows the printed multilayer stack of Ag/Al_2O_3/Ag. STEM and SEM images of both un-sintered and sintered nanoparticles of Ag and Al_2O_3 can be found in Supporting Information **Figure S3**. After printing, the circuit electronics component, including the M24LR04E IC, AT-Tiny 85, two 1KΩ resistors, and two LEDs were mounted on the printed flexible circuits, as shown in **Figure 7d**. The printed device was powered by a 3.3v coin cell battery. This circuit used the printed NFC antenna along with NFC IC and AT-Tiny 85 microcontroller to read the NFC Data Exchange Format (NDEF) message from a phone via NFC program to control two output LED's (Supporting Information **Figure 7e, f**).

The expected operation of the circuit showed that the printed insulating Al_2O_3 layer completely isolated the bottom and top metal layers. Also, the crossed-over Ag lines were highly conductive and the resistance of Ag before and after printing Al_2O_3 showed no noticeable changes. The video of the working device is demonstrated in supporting information, **Video S2**. Furthermore, using this printing method, by controlling the printing conditions, vertical interconnects that can bridge different heights can be fabricated (Supporting Information **Figure S4**). The test results confirmed that separate multilevel metal interconnects were successfully formed.

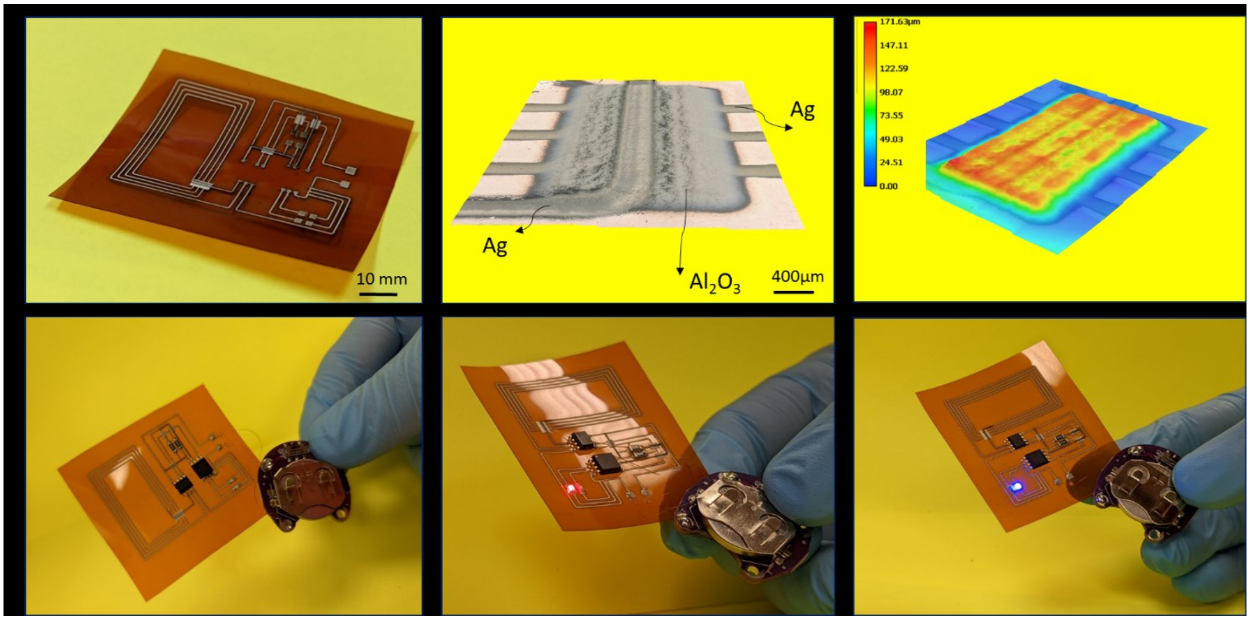

Figure 7. Digital photo of the M-ANM printed lines of flexible hybrid electronics (**a**). 3D optical image of the printed Al_2O_3 as the isolator layer between crossed Ag lines of the NFC antenna (**b**). The height profile image printed Al_2O_3 section in the NFC antenna with a thickness of ~140 µm (**c**). Completed flexible hybrid electronic circuit with all mounted components (**d**). Digital photo of the circuit showing the red (**e**) or blue (**f**) LED switching via NFC communication controlled by a mobile phone.

Conclusion

In summary, we developed a new dry multimaterial printing technique that is capable of printing multiple materials side-by-side and layer-by-layer. The unique feature of this technique was the generation of dry and pure nanoparticles through pulsed laser ablation of solid targets. The generated nanoparticles directly exited from the nozzle toward the substrate, where they were sintered by a real-time laser sintering process at room temperature and atmospheric pressure. A target carousel holding multiple targets was used to bring different targets in engagement with the ablation laser beam to print multiple materials. To demonstrate the capability, ZnO photodetectors with Ag electrodes and multimaterial Ag-Al_2O_3 FHE circuits were printed and tested. This versatile and unique M-ANM printing technique was used to print a variety of materials such as Ag, BTO, TiO_2, SnO, ZnO, and Al_2O_3 that could be used for broad applications ranging from flexible electronics, optoelectronics, energy storage and harvesting, space, and medical applications enabling the future internet of things (IoT).

Methods and Characterizations

Electrical measurements: Four-probe measurements were performed to obtain the resistance of printed lines using a Keithley 2400 as a current generator and as a voltmeter.

Micro and nanoscale imaging: SEM and STEM images were obtained using Zeiss Crossbeam 550 microscope. Nanoparticles were directly deposited onto the TEM grid by holding the TEM grids under the printer nozzle for a few seconds.

Optical Imaging: KEYENCE VHX-6000 series microscope was used to measure the thickness of ANM-printed samples.

Photodetector characterization: Photodetectors were mounted onto a homebuilt holder and connected to the source-meter unit (Keithley 2400, Tektronix, Inc.) using two probes. The current changes in the devices were measured under various optical illumination powers using a 405 nm laser light source. Experiments were done under ambient conditions and at room temperature.

Flexible hybrid electronics: The antenna, along with the NFC IC read the data from the phone and transfers it over Inter-Integrated Circuit (I2C) ports. The AT-Tiny 85 along with the TinyWire library, which acts as I2C master simulates the pins port-b (PB2) and PB0 as the serial clock (SCL) and serial data (SDA), respectively. Basically, the AT-Tiny here acts as the I2C master, while the NFC IC acts as the slave. Then after the AT-Tiny 85 decodes the data bits and, depending on the decimal value, it controls the output pins on which LEDs are connected.

Acknowledgments

This material is based upon work partially supported by the U.S. National Science Foundation (NSF) under grants No. 1923363, No. 2134024, and No. 2018794. Alabama Micro/Nanoelectronic Science and Technology Center (AMNSTC) at Auburn University provided access to the electrical measurement facility.

Conflict of Interest

The authors declare no conflict of interest.

Author Contributions

Z.A. designed and performed the experimental setup, synthesis and processing experiments, materials characterization, data analysis, and manuscript writing. A.P. participated in reliability tests and performance analysis. A. T. performed the Raman measurements and analysis and participated in reliability tests and analysis. S. J. performed the XRD measurement and analysis. S.L. participated in the SEM and STEM imaging and data analysis. N.S. participated in design of experiments, data analysis, and discussions. M.M.S. led the project, participated in experimental design, data acquisition and analysis, discussions, and manuscript preparation. All of the authors participated in manuscript preparation and revision processes.

Supporting Information

Supporting information is available online. Multiple stages of multimaterial antenna printing, multiple stages of multimaterial FHE circuit printing, STEM images of Ag and Al_2O_3 nanoparticles, optical images of the printed Al_2O_3 as the isolating layers between the crossed Ag lines, video of the working antenna, video of the working FHE circuit.

References

1. D. Corzo, G. Tostado-Blázquez and D. Baran, *Flexible Electronics: Status, Challenges and Opportunities.* Frontiers in Electronics, 2020. **1**, p.594003.
2. H. Liu, H. Zhang, W. Han, H. Lin, R. Li, J. Zhu and W. Huang, *3D Printed Flexible Strain Sensors: From Printing to Devices and Signals.* Advanced Materials, 2021. **33**(8), p.2004782.
3. G.C. Righini, J. Krzak, A. Lukowiak, G. Macrelli, S. Varas and M. Ferrari, *From flexible electronics to flexible photonics: A brief overview.* Optical Materials, 2021. **115**, p.111011.

4. P. Giannakou, M.G. Masteghin, R.C.T. Slade, S.J. Hinder and M. Shkunov, *Energy storage on demand: ultra-high-rate and high-energy-density inkjet-printed NiO micro-supercapacitors.* Journal of Materials Chemistry A, 2019. **7**(37): p. 21496-21506.
5. R. Šakalys, B.S. Mohammadlou and R. Raghavendra, *Fabrication of multi-material electronic components applying non-contact printing technologies: A review.* Results in Engineering, 2022. **15**, p.100578.
6. A. Renteria, V.H. Balcorta, C. Marquez, A.A. Rodriguez, I. Renteria-Marquez, J. Regis, B. Wilburn, S. Patterson, D. Espalin, T.-L. Tseng and Y. Lin, *Direct ink write multi-material printing of PDMS-BTO composites with MWCNT electrodes for flexible force sensors.* Flexible and Printed Electronics, 2022. **7**(1), p.015001.
7. J. Wu, H. Pang, L. Ding, Y. Wang, X. He, Q. Shu, S. Xuan and X. Gong, *A lightweight, ultrathin aramid-based flexible sensor using a combined inkjet printing and buckling strategy.* Chemical Engineering Journal, 2021. **421**, p.129830.
8. Z. Ahmadi, P. Fathi-Hafshejani, E. Kayali, M. Beidaghi and M. Mahjouri-Samani, *Rapid laser nanomanufacturing and direct patterning of 2D materials on flexible substrates—2DFlex.* Nanotechnology, 2020. **32**(5), p.055302.
9. N. Gholizadeh, J.M. Hood and R.A. Dougal, *Evaluation of Linear Implicit Quantized State System method for analyzing mission performance of power systems.* The Journal of Defense Modeling and Simulation: Applications, Methodology, Technology, 2021. **20**(2): p. 159-170.
10. S. Choi, H. Lee, R. Ghaffari, T. Hyeon and D.-H. Kim, *Recent Advances in Flexible and Stretchable Bio-Electronic Devices Integrated with Nanomaterials.* Advanced Materials, 2016. **28**(22): p. 4203-4218.
11. J.A. Rogers, T. Someya and Y. Huang, *Materials and Mechanics for Stretchable Electronics.* Science, 2010. **327**(5973): p. 1603-1607.
12. S. Ma, Y. Kumaresan, A.S. Dahiya and R. Dahiya, *Ultra-Thin Chips with Printed Interconnects on Flexible Foils.* Advanced Electronic Materials, 2021. **8**(5), p.2101029.
13. N. Divakaran, J.P. Das, A.K. P V, S. Mohanty, A. Ramadoss and S.K. Nayak, *Comprehensive review on various additive manufacturing techniques and its implementation in electronic devices.* Journal of Manufacturing Systems, 2022. **62**: p. 477-502.
14. X.C. Li, L. Yao, W. Song, F. Liu, Q. Wang, J. Chen, Q. Xue and W.Y. Lai, *Intrinsically Stretchable Electroluminescent Elastomers with Self-Confinement Effect for Highly Efficient Non-Blended Stretchable OLEDs.* Angewandte Chemie International Edition, 2022. **62**(2), p.e202213749.
15. Y. Gong, Y.-Z. Zhang, S. Fang, C. Liu, J. Niu, G. Li, F. Li, X. Li, T. Cheng and W.-Y. Lai, *Artificial intelligent optoelectronic skin with anisotropic electrical and optical responses for multi-dimensional sensing.* Applied Physics Reviews, 2022. **9**(2), p. 021403.
16. C. Wei and L. Li, *Recent progress and scientific challenges in multi-material additive manufacturing via laser-based powder bed fusion.* Virtual and Physical Prototyping, 2021. **16**(3): p. 347-371.
17. L. Nayak, S. Mohanty, S.K. Nayak and A. Ramadoss, *A review on inkjet printing of nanoparticle inks for flexible electronics.* Journal of Materials Chemistry C, 2019. **7**(29): p. 8771-8795.
18. V. Beedasy and P.J. Smith, *Printed Electronics as Prepared by Inkjet Printing.* Materials, 2020. **13**(3), pp.8771-8795.

19. A. Sajedi-Moghaddam, E. Rahmanian and N. Naseri, *Inkjet-Printing Technology for Supercapacitor Application: Current State and Perspectives.* ACS Applied Materials & Interfaces, 2020. **12**(31): p. 34487-34504.
20. S. Lu, J.A. Cardenas, R. Worsley, N.X. Williams, J.B. Andrews, C. Casiraghi and A.D. Franklin, *Flexible, Print-in-Place 1D–2D Thin-Film Transistors Using Aerosol Jet Printing.* ACS Nano, 2019. **13**(10): p. 11263-11272.
21. E. MacDonald and R. Wicker, *Multiprocess 3D printing for increasing component functionality.* Science, 2016. **353**(6307), p.aaf2093.
22. Z. Ahmadi, S. Lee, R.R. Unocic, N. Shamsaei and M. Mahjouri-Samani, *Additive Nanomanufacturing of Multifunctional Materials and Patterned Structures: A Novel Laser-Based Dry Printing Process.* Advanced Materials Technologies, 2021. **6**(5), p.2001260.
23. Z. Ahmadi, S. Lee, A. Patel, R.R. Unocic, N. Shamsaei and M. Mahjouri-Samani, *Dry Printing and Additive Nanomanufacturing of Flexible Hybrid Electronics and Sensors.* Advanced Materials Interfaces, 2022. **9**(12), p.2102569.
24. Z. Ahmadi, S. Lee, R.R. Unocic, N. Shamsaei, M. Mahjouri-Samani, A.V. Kabashin, M. Farsari and M. Mahjouri-Samani, *Laser-based additive nanomanufacturing of functional hybrid materials, structures, and devices*, in *Nanoscale and Quantum Materials: From Synthesis and Laser Processing to Applications 2022*, p. PC119900A. SPIE, 2022.
25. H.W. Tan, Y.Y.C. Choong, C.N. Kuo, H.Y. Low and C.K. Chua, *3D printed electronics: Processes, materials and future trends.* Progress in Materials Science, 2022. **127**, p.100945.
26. L. Jaksa, D. Pahr, G. Kronreif and A. Lorenz, *Development of a Multi-Material 3D Printer for Functional Anatomic Models.* International Journal of Bioprinting, 2021. **7**(4), p. 420.
27. R. Bernasconi, D. Hatami, H.N. Hosseinabadi, V. Zega, A. Corigliano, R. Suriano, M. Levi, G. Langfelder and L. Magagnin, *Hybrid additive manufacturing of a piezopolymer-based inertial sensor.* Additive Manufacturing, 2022. **59**, p.103091.
28. Y. Li, R. Wang, X. Zhu, J. Yang, L. Zhou, S. Shang, P. Sun, W. Ge, Q. Xu and H. Lan, *Multinozzle 3D Printing of Multilayer and Thin Flexible Electronics.* Advanced Engineering Materials, 2022, p.2200785.
29. W.Y. Yeong, G.L. Goh, G.D. Goh, S. Lee, J. Altherr, J. Tan and D. Campolo, *3D printing of soft grippers with multimaterial design: Towards shape conformance and tunable rigidity.* Materials Today: Proceedings, 2022, p 525-530.
30. R. Wick-Joliat, M. Schroffenegger and D. Penner, *Multi-material ceramic material extrusion 3D printing with granulated injection molding feedstocks.* Ceramics International, 2022, pp.6361-6367.
31. S. Tibbits, *4D Printing: Multi-Material Shape Change.* Architectural Design, 2014. **84**(1): p. 116-121.
32. L.R. Lopes, A.F. Silva and O.S. Carneiro, *Multi-material 3D printing: The relevance of materials affinity on the boundary interface performance.* Additive Manufacturing, 2018. **23**: p. 45-52.
33. D. Wang, L. Liu, G. Deng, C. Deng, Y. Bai, Y. Yang, W. Wu, J. Chen, Y. Liu, Y. Wang, X. Lin and C. Han, *Recent progress on additive manufacturing of multi-material structures with laser powder bed fusion.* Virtual and Physical Prototyping, 2022. **17**(2): p. 329-365.
34. U. Shaukat, E. Rossegger and S. Schlögl, *A Review of Multi-Material 3D Printing of Functional Materials via Vat Photopolymerization.* Polymers, 2022. **14**(12), p.2449.

35. B. Grigoryan, D.W. Sazer, A. Avila, J.L. Albritton, A. Padhye, A.H. Ta, P.T. Greenfield, D.L. Gibbons and J.S. Miller, *Development, characterization, and applications of multi-material stereolithography bioprinting.* Scientific Reports, 2021. **11**(1), p. 3171.
36. D. Chen and X. Zheng, *Multi-material Additive Manufacturing of Metamaterials with Giant, Tailorable Negative Poisson's Ratios.* Scientific Reports, 2018. **8**(1), pp.1-8.
37. A.C. Lamont, M.A. Restaino, M.J. Kim and R.D. Sochol, *A facile multi-material direct laser writing strategy.* Lab on a Chip, 2019. **19**(14): p. 2340-2345.
38. A.D. Valentine, T.A. Busbee, J.W. Boley, J.R. Raney, A. Chortos, A. Kotikian, J.D. Berrigan, M.F. Durstock and J.A. Lewis, *Hybrid 3D Printing of Soft Electronics.* Advanced Materials, 2017. **29**(40), p.1703817.
39. G.L. Goh, H. Zhang, T.H. Chong and W.Y. Yeong, *3D Printing of Multilayered and Multimaterial Electronics: A Review.* Advanced Electronic Materials, 2021. **7**(10), p.2100445.
40. M.A. Skylar-Scott, J. Mueller, C.W. Visser and J.A. Lewis, *Voxelated soft matter via multimaterial multinozzle 3D printing.* Nature, 2019. **575**(7782): p. 330-335.
41. W. Liu, Y.S. Zhang, M.A. Heinrich, F. De Ferrari, H.L. Jang, S.M. Bakht, M.M. Alvarez, J. Yang, Y.-C. Li, G. Trujillo-de Santiago, A.K. Miri, K. Zhu, P. Khoshakhlagh, G. Prakash, H. Cheng, X. Guan, Z. Zhong, J. Ju, G.H. Zhu, X. Jin, S.R. Shin, M.R. Dokmeci, and A. Khademhosseini, *Rapid Continuous Multimaterial Extrusion Bioprinting.* Advanced Materials, 2017. **29**(3), p.1604630.
42. K. Sun, T.-S. Wei, B.Y. Ahn, J.Y. Seo, S.J. Dillon and J.A. Lewis, *3D Printing of Interdigitated Li-Ion Microbattery Architectures.* Advanced Materials, 2013. **25**(33): p. 4539-4543.
43. J.J. Adams, E.B. Duoss, T.F. Malkowski, M.J. Motala, B.Y. Ahn, R.G. Nuzzo, J.T. Bernhard and J.A. Lewis, *Conformal Printing of Electrically Small Antennas on Three-Dimensional Surfaces.* Advanced Materials, 2011. **23**(11): p. 1335-1340.
44. J.T. Muth, D.M. Vogt, R.L. Truby, Y. Mengüç, D.B. Kolesky, R.J. Wood and J.A. Lewis, *Embedded 3D Printing of Strain Sensors within Highly Stretchable Elastomers.* Advanced Materials, 2014. **26**(36): p. 6307-6312.
45. B.G. Compton and J.A. Lewis, *3D Printing: 3D-Printing of Lightweight Cellular Composites (Adv. Mater. 34/2014).* Advanced Materials, 2014. **26**(34): p. 6043-6043.
46. D.B. Kolesky, R.L. Truby, A.S. Gladman, T.A. Busbee, K.A. Homan and J.A. Lewis, *3D Bioprinting of Vascularized, Heterogeneous Cell-Laden Tissue Constructs.* Advanced Materials, 2014. **26**(19): p. 3124-3130.
47. C.J. Hansen, R. Saksena, D.B. Kolesky, J.J. Vericella, S.J. Kranz, G.P. Muldowney, K.T. Christensen and J.A. Lewis, *High-Throughput Printing via Microvascular Multinozzle Arrays.* Advanced Materials, 2013. **25**(1): p. 96-102.
48. D.J. Lorang, D. Tanaka, C.M. Spadaccini, K.A. Rose, N.J. Cherepy and J.A. Lewis, *Photocurable Liquid Core-Fugitive Shell Printing of Optical Waveguides.* Advanced Materials, 2011. **23**(43): p. 5055-5058.
49. J.O. Hardin, T.J. Ober, A.D. Valentine and J.A. Lewis, *Microfluidic Printheads for Multimaterial 3D Printing of Viscoelastic Inks.* Advanced Materials, 2015. **27**(21): p. 3279-3284.
50. W.C. Liu, V.H.Y. Chou, R.P. Behera and H. Le Ferrand, *Magnetically assisted drop-on-demand 3D printing of microstructured multimaterial composites.* Nature Communications, 2022. **13**(1), p.5015.

51. R. Hensleigh, H. Cui, Z. Xu, J. Massman, D. Yao, J. Berrigan and X. Zheng, *Charge-programmed three-dimensional printing for multi-material electronic devices.* Nature Electronics, 2020. **3**(4): p. 216-224.
52. V.-T. Tran, Y. Wei and H. Du, *On-Substrate Joule Effect Heating by Printed Micro-Heater for the Preparation of ZnO Semiconductor Thin Film.* Micromachines, 2020. **11**(5), p.490.
53. C. Zhang, L. McKeon, M.P. Kremer, S.-H. Park, O. Ronan, A. Seral-Ascaso, S. Barwich, C.Ó. Coileáin, N. McEvoy, H.C. Nerl, B. Anasori, J.N. Coleman, Y. Gogotsi and V. Nicolosi, *Additive-free MXene inks and direct printing of micro-supercapacitors.* Nature Communications, 2019. **10**(1), p.1795.
54. F. Zacharatos, M. Makrygianni and I. Zergioti, *Laser-Induced Forward Transfer (LIFT) Technique as an Alternative for Assembly and Packaging of Electronic Components.* IEEE Journal of Selected Topics in Quantum Electronics, 2021. **27**(6): p. 1-8.
55. S.H. Park, R. Su, J. Jeong, S.Z. Guo, K. Qiu, D. Joung, F. Meng and M.C. McAlpine, *3D Printed Polymer Photodetectors.* Advanced Materials, 2018. **30**(40), p.1803980.
56. Y. Khan, A. Thielens, S. Muin, J. Ting, C. Baumbauer and A.C. Arias, *A New Frontier of Printed Electronics: Flexible Hybrid Electronics.* Advanced Materials, 2019. **32**(15), p.1905279.

TOC

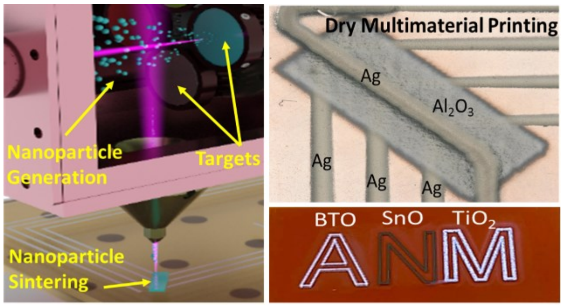
Nanoparticle Generation
Targets
Nanoparticle Sintering
Dry Multimaterial Printing
Ag
Al_2O_3
Ag
Ag
Ag
BTO
SnO
TiO_2